Mapping Glacier Elevations and Their Changes in the Western Qilian Mountains, Northern Tibetan Plateau, by Bistatic InSAR

Article *in* IEEE Journal of Selected Topics in Applied Earth Observations and Remote Sensing · October 2017

DOI: 10.1109/JSTARS.2017.2764751

6 authors, including:

Yafei Sun
Institute of Geodesy and Geophysics, CAS
11 PUBLICATIONS **28** CITATIONS
SEE PROFILE

Liming Jiang
Institute of Geodesy and Geophysics, Chinese Academy of Sciences, Wuhan, China
77 PUBLICATIONS **675** CITATIONS
SEE PROFILE

Lin Liu
Chinese Academy of Sciences
17 PUBLICATIONS **38** CITATIONS
SEE PROFILE

Sun Qishi
Chinese Academy of Sciences
7 PUBLICATIONS **16** CITATIONS
SEE PROFILE

Mapping Glacier Elevations and Their Changes in the Western Qilian Mountains, Northern Tibetan Plateau, by Bistatic InSAR

Yafei Sun, Liming Jiang, Lin Liu, Qishi Sun, Hansheng Wang, and Houtse Hsu

***Abstract*—Accurate measurements of glacier surface topography and their changes play an essential role in various glaciological studies related to glacier dynamics and mass balance. The focus of this study is on mapping glacier digital elevation model (DEM) and elevation changes in the western Qilian Mountains, northern Tibetan Plateau, by synergistically using the TanDEM-X (TDX) bistatic Interferometric Synthetic Aperture Radar (InSAR) data in 2013 and Shuttle Radar Topography Mission (SRTM) DEM in 2000. The first high-resolution and high-precision glacier DEM is derived in this region by a TDX InSAR procedure with a nonlocal (NL) filter. Validated against the Ice, Cloud, and land Elevation Satellite height references, the absolute height error of the TanDEM-X DEM derived with the NL filter and the Goldstein filter with the parameters investigated is, respectively, 1.493 ± 0.747 and 1.857 ± 1.709 m. Further, four combinations of differential phase method (DiffPha) and DEM differencing method (DiffDem) with Goldstein filter and NL filter are applied to estimate glacier elevation changes between 2000 and 2013. The synergistic use of the DiffPha method and the NL filter is superior to other three combinations in terms of uncertainty and noise reduction. Generally, a clear surface thinning can be found in most glacier tongue regions, the maximum value of elevation lowering up to approximately -40 m, whereas a slight thickening is detected in accumulation areas, which are in agreement with the height difference results between GPS measurements and SRTM DEM over Laohugou Glacier No.12. This study demonstrates the potential of the TanDEM-X bistatic InSAR in mapping surface topography and elevation changes of valley glaciers in the Tibetan Plateau.**

Manuscript received November 1, 2016; revised March 11, 2017, June 16, 2017, and October 8, 2017; accepted October 12, 2017. This work was supported in part by the National Key R & D Program of China under Grant 2017YFA0603103, in part by the National Natural Science Foundation of China under Grant 41431070, Grant 41590854, and Grant 41621091, in part by the Key Research Program of Frontier Sciences, CAS under Grant QYZDB-SSW-DQC027 and Grant QYZDJ-SSW-DQC042, and in part by the DLR by providing the TanDEM-X data used via the TanDEM-X AO under Project XTI_LAND0413. *(Corresponding author: Liming Jiang.)*

Y. Sun, L. Jiang, and Q. Sun are with the State Key Laboratory of Geodesy and Earth's Dynamics, Institute of Geodesy and Geophysics, CAS, Wuhan 430077, China, and also with the University of Chinese Academy of Sciences, Beijing 100049, China (e-mail: sunyafei@whigg.ac.cn; jlm@whigg.ac.cn; sunqishi14@mails.ucas.ac.cn).

L. Liu is with the MOE Key Laboratory of Fundamental Physical Quantities Measurement, Hubei Key Laboratory of Gravitation and Quantum Physics, School of Physics, Huazhong University of Science and Technology, Wuhan 430074, China (e-mail: liulin@whigg.ac.cn).

H. Wang and H. Hsu are with the State Key Laboratory of Geodesy and Earth's Dynamics, Institute of Geodesy and Geophysics, CAS, Wuhan 430077, China (e-mail: whs@whigg.ac.cn; hsuh@whigg.ac.cn).

Color versions of one or more of the figures in this paper are available online at http://ieeexplore.ieee.org.

Digital Object Identifier 10.1109/JSTARS.2017.2764751

***Index Terms*—Bistatic InSAR, glacier DEM, glacier elevation change, Tibetan plateau, western Qilian mountains.**

I. Introduction

ACCURATE measurements of glacier surface topography play an essential role in various glaciological studies related to glacier dynamics and mass balance. The applications of digital elevation models (DEMs) for glacier topographic parameters calculation, ice-flow velocity extraction, debris-covered glacier detection are widely discussed in literatures [1]–[3]. In particular, the advent of advanced remote sensing techniques enables glacier DEMs generation from space with high resolution, global coverage, and low cost. Therefore, multitemporal glacier DEMs acquired at different times are increasingly required for a robust estimation of glacier thickness change and mass balance in mountain glaciated regions at local through global scales [4], [5].

Over the past decades, high-resolution remote sensing data acquired by various aerial and satellite platforms have been considerably exploited to generate and update topographic information over glaciated regions. They are basically grouped into three categories: 1) optical stereo image pairs, 2) laser scanning (LiDAR) point clouds, and 3) Interferometric Synthetic Aperture Radar (InSAR) imagery. Terrestrial, aerial, and satellite optical stereo image pairs from different viewing angles can be utilized to derive DEMs with digital photogrammetric techniques, which depend on knowledge of the exact image and terrain geometries at the time of acquisition. A large number of studies have reported on the generation of DEMs and topographic changes from optical stereo pairs for glaciological applications, especially from satellite remote sensing images including Terra-ASTER [4], [6], SPOT5-HRS [7], ALOS-PRISM [8], Corona series [4], [8], and ZIYUAN-3 [9]. A major challenge in using digital photogrammetry to map glacier surface topography is that the glacier surface should have sufficient radiometric and/or topographic heterogeneity in image pairs. Otherwise, it can cause either null values or erroneous elevation estimates especially over debris-free ice or firn areas. In addition, frequent cloud cover is another obstacle to optical remote sensing of mountainous and cold areas [10]. Ground-based and airborne LiDAR systems, producing extremely dense three-dimensional point clouds, are important operational tools for measuring

high-resolution glacier surface topography and have been increasingly utilized in glacial geo-morphological investigations [11]. However, it is difficult for these LiDAR systems to acquire topographic datasets over large-scale glaciated regions, because of political sensitivities (e.g., Karakoram), high costs, and poor archiving.

SAR interferometry has been proven to be one of the most valuable remote sensing technologies for mapping the earth topography, by exploiting the phase difference between two independent SAR image acquisitions that is very sensitive to topographic variations to derive DEMs with very high accuracy [12]. Glacier DEMs have been successfully derived using a range of SAR sources mostly acquired with repeat-pass imaging modes, including ERS-1/2 [13], Radarsat-1/2 [14], ALOS/PALSAR [15], and sensors onboard fixed-wing aircraft [16]. However, this repeat-pass InSAR is still challenging for glacier applications because it commonly suffers from atmospheric disturbance (mainly due to variations of the troposphere and the ionosphere between the repeat-pass SAR acquisitions), as well as temporal decorrelation induced by ice melting, snow accumulation and glacier movement between acquisitions [17]. In contrast, a bistatic interferometric system can overcome the limitations in repeat-pass interferometry. The Shuttle Radar Topography Mission (SRTM) flown in February 2000, which was the first single-pass space-borne InSAR system, provided highly valuable DEM products covering continental areas from 56°S and 60°N with 1 and 3 arcsec spatial resolutions (approximately 30 and 90 m, respectively) [18]. It is noteworthy that the TanDEM-X mission, launched in 2010 by the German Aerospace Center (DLR), opens a new era in single-pass satellite SAR remote sensing. The TanDEM-X (TDX) mission employs a bistatic interferometric configuration of the two identical satellites TerraSAR-X (TSX) and TDX flying in a closely controlled formation, the primary objective of which is to generate a global, high-accurate, and homogeneous DEM following the high standard accuracy HRTI-3 [19]. Recently, several previous studies have used the TanDEM-X bistatic SAR data to investigate ice surface topography and mass balance in the Tibetan Plateau [20]–[23], the central Tien Shan [24], the western Alps [25], and the Antarctic Peninsula [26].

This study aims to quantitatively evaluate the potential of the TDX bistatic SAR data for measuring glacier surface topography and elevation changes over mountain regions. A case study was carried out over valley glaciers in the western Qilian Mountain, northern Tibetan Plateau. A high-resolution and high-precision glacier DEM was derived from a pair of TSX/TDX bistatic SAR data acquired in 2013 and validated by Ice, Cloud, and land Elevation Satellite (ICESat) elevation data. Additionally, we employed a differential phase method (hereinafter referred to as DiffPha) and a DEM differencing method (hereinafter referred to as DiffDem) to this TDX DEM and the SRTM DEM in 2000 to estimate 2000–2013 glacier elevation changes in the study area. Finally, the results were compared with elevation differences between GPS measurements and the SRTM DEM.

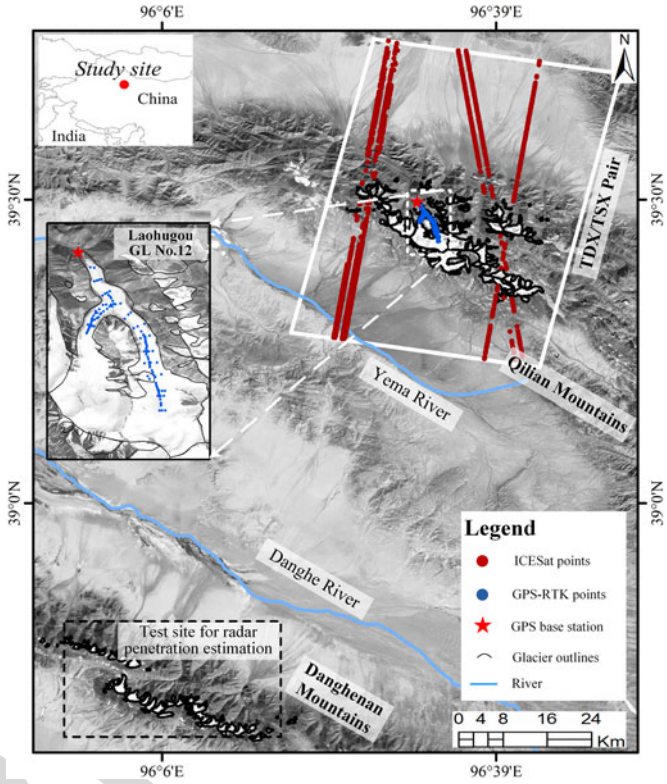

Fig. 1. Location of study area and data used. The TDX/TSX SAR images and the glacial boundary coverage are represented with white rectangle and black polygon, respectively. The Yema and Danghe rivers are shown as blue solid lines. ICESat points and GPS-RTK points are indicated as red dots and blue dots, respectively. The illustration of GPS measurement distribution in the Laohugou No.12 is shown in the inset left part. The location of GPS base station is shown as red pentagram. The location of the test site for radar penetration estimation is also shown in Fig. 1, which is located 90 km southeast of the study area. The background is an optical image acquired from Google Earth.

II. Study Area and Data

A. Study Area

The study area (39°12'–39°36' N, 96°18'–96°45' E), located in the western Qilian Mountains (see Fig. 1), northern Tibetan Plateau, is home to a total of 216 glaciers with an area of more than 134.9 km^2 and an ice volume of about 7.6 km^3 [27]. The glacier elevations range from 4000 to 5500 m a.s.l. with a mean equilibrium-line altitude of 4830 m a.s.l. [28]–[30]. Laohugou Glacier No.12 is the longest and largest valley glacier in this region that stretches approximately 10.8 km and covers a total area of more than 20.4 km^2 [28].

The continental, arid climate of the study area is dominated by the Siberian anticyclone and by westerlies [28], [31]. Annual mean air temperature and snow surface temperature are −12.0 °C and −16.9 °C, respectively. Monthly air temperature and precipitation data show strong seasonal variation, with more than 70% of precipitation falling from May to September [28]. On 21 November 2013 when the TanDEM-X bistatic data were acquired for this study, the average daily air temperature and relative humidity are −15.6 °C and 47% recorded by the automatic weather station on the Laohugou Glacier No.12, which is

TABLE I
MAIN PARAMETERS OF THE TSX/TDX DATA PAIR USED

Parameters	Description
Acquisition Modes	Bistatic Mode
Imaging Modes	Strip-map
Product format	CoSSC
Polarization	HH
Orbit direction	Descending
Looking direction	Right
Temporal baseline (s)	0
Perpendicular baseline (m)	154.85
Height of ambiguity (m)	33.03
Central incidence angle (°)	33.83
Range resolution (m)	3.2
Azimuth resolution (m)	3.3
Number of multilooks	5
Average coherence	0.86
Interferogram resolution (m)	10

located in the ablation area at 4550 m a.s.l. [32]. Personal communication with Wang, 2016 and his published study suggest that in November (the beginning of the accumulation season) the glacier surface is usually covered by shallow dry snow which is underlay by compacted snow or firn layer [33]. In addition, the fresh snow depths in the specific period of the SAR acquisitions ranged from 10 to 50 cm recorded by stake measurements which were located in an elevation span of 4355–4990 m a.s.l. [33], and were generally depended on altitudes. The glaciers in this region are relatively stable compared to glaciers in Himalayan Mountains, however, recent studies have shown that the regional climate tends to become warmer and moister, and the glaciers are shrinking [34]. The area of the Laohugou Glacier No.12 gradually diminished from 1957 to 2009 [35]. And this glacier experienced significant thinning but slight thickening in part of the accumulation zone [28].

B. Dataset Used

1) TanDEM-X Bistatic SAR Data: In this study, one pair of TSX/TDX SAR data in bistatic strip-map mode acquired on 21 November 2013 was used to generate high-resolution and high-precision TDX DEM. The data format is Coregistered Single-look Slant-range Complex (CoSSC), which has already been processed by Integrated TanDEM Processor from DLR [36]. The bistatic SAR data were acquired in a descending track and HH polarization with a central incidence angle of 33.83°. The spatial resolution in range and azimuth direction is 3.2 and 3.3 m, respectively. The two satellites have a temporal baseline of approximately 0 s flying in a close helix formation. The main parameters of the TSX/TDX data were summarized in Table I.

2) SRTM DEMs: The SRTM employed two SAR systems, one C band system (wavelength of 5.6 cm, SRTM-C radar) and another X band system (wavelength of 3.1 cm, SRTM-X radar). SRTM-C radar generated DEMs of contiguous mapping coverage with 1 and 3 arc s spatial resolution (about 30 and 90 m), however, SRTM-X radar only acquired DEMs along discrete swaths 50 km wide with 1 arc s spatial resolution [18]. Over nonglacierized areas, the initial mission specifications in terms of vertical accuracy (±16 m linear error at the 90% confidence level) are fulfilled [37]. Only a few studies considered SRTM in a glacial environment, for the Gruben area (Swiss Alps), Kääb (2005) found a standard deviation of ±20 m for SRTM (3 arc s) and indicated that the 1 arc s DEM might have an accuracy of 7 m on average [38]. Recently, a mean and standard deviation of elevation differences of 1.03 ± 15.20 m over glacier areas in the eastern Tibetan Plateau by comparing ICESat and SRTM-C (3 arc s) elevation measurements in this literature [39].

In this study, the SRTM-C DEM with 1 arc s spatial resolution (about 30 m) was used to generate simulated topographic phase and to estimate glacier elevation changes with TanDEM-X InSAR data. This DEM version was released in 2015 by U.S. Geological Survey (USGS) and can be downloaded from https://lta.cr.usgs.gov/SRTM1Arc. Since the SRTM-X DEM is not available over our study area, a pair of SRTM-C/X DEMs over glacier areas, which located at 90 km southwest of the study area, were selected to statistically estimate DEM differences of the C-band and X-band radar signals into snow and ice. This radar penetration difference was used to correct the elevation changes derived from the SRTM-C and TDX DEMs.

3) Height Reference Datasets: ICESat laser altimeter data were used as height reference data to assess vertical accuracy of the InSAR-derived TDX DEM in 2013. The geographic distribution of the ICESat footprints was shown in Fig. 1. The geo-science laser altimeter system instrument aboard the ICESat measures land elevations with the footprints of 70 m in diameter and 170 m intervals in along-track [40]. ICESat elevation data have an accuracy on an order of 0.1 m (1 σ) in the region of flat bald, but it can degrade to values on an order of 1 m (1 σ) in the region of irregular and rugged land surface [41]. In this study, 90% of the ICESat measurements from 2003 to 2009 were located in flat and bald regions, whereas the other 10% in irregular and rugged areas. Moreover, although a few of ICESat footprints were situated on glacier surface, possible ice elevation changes occurred during the period from 2009 to 2013. Therefore, only ICESat measurements located in flat off-glacier areas were utilized for accuracy assessment (see Fig. 1).

In addition, we carried out a GPS-RTK (real-time kinematic) surveying campaign over Laohugou Glacier No.12 in late September of 2012. The GPS instruments we used are the dual-frequency South Lingrui S82 and Trimble 5700, and the location of base station was shown in Fig. 1. A total of 121 GPS points (see Fig. 1) were surveyed and obtained high-accuracy glacier elevation measurements (vertical precision of ±0.2 m). These GPS measurements were employed to estimate glacier elevation changes compared with SRTM-C DEM in 2000 to evaluate elevation changes between the SRTM-C and TDX DEMs.

III. METHODS

A. DEM Generation With TanDEM-X InSAR

Interferometric phase (φ_{int}) can be schematically expressed as the sum of components [see (1)] contributed by the topography (φ_{topo}), the line of sight surface motion between the two acquisition times (φ_{disp}), the atmospheric distortions (φ_{atm}), the inaccurate orbit state vectors ($\varphi_{\mathrm{orbital}}$), and a random noise

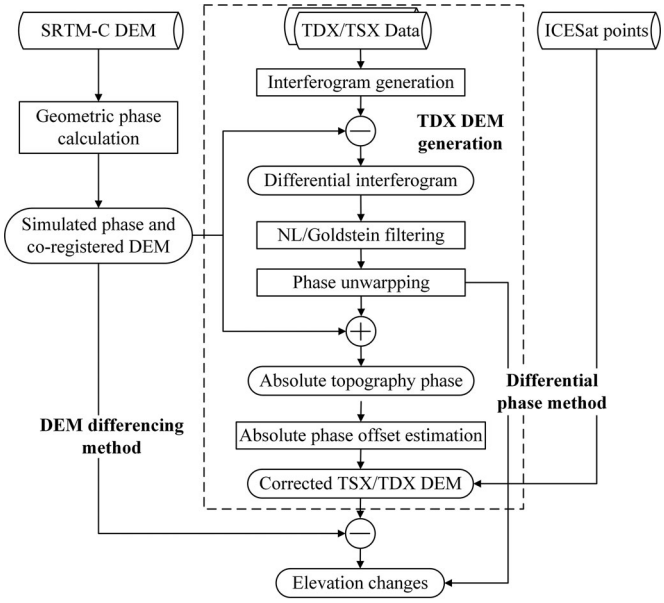

Fig. 2. Flowchart of TanDEM-X DEM generation and glacier elevation change estimation. The processing steps of TanDEM-X DEM generation are shown with the dotted box, and two different methods to estimate glacier elevation changes are labeled in the flowchart.

term $(\varphi_{\mathrm{noise}})$ related to temporal decorrelation, image misregistration and other random instrumental noises [42]

$$\varphi_{\mathrm{int}} = \varphi_{\mathrm{topo}} + \varphi_{\mathrm{disp}} + \varphi_{\mathrm{atm}} + \varphi_{\mathrm{orbital}} + \varphi_{\mathrm{noise}}. \quad (1)$$

For TSX/TDX satellites flying in close formation that uses either TSX or TDX as a transmitter to illuminate a radar signal on the earth's surface, the scattered radar signals are recorded by both satellites simultaneously. This simultaneous data acquisition can minimize the interferometric phase of temporal decorrelation and atmospheric disturbance. Additionally, rainfall (particularly heavy precipitation in a weather event) might affect X-band radar signal, however, for our case very little precipitation occurs in the study area in winter [28]. Therefore, the influence of phase terms of φ_{disp} and φ_{atm} can be neglected in TSX/TDX bistatic interferometry. Also, the impact of the phase $\varphi_{\mathrm{orbital}}$ can be reduced by the step of baseline refinement in the data processing [43].

In this study, unlike a common InSAR method widely used to generate a DEM in which an interferogram is directly unwrapped and then surface height is calculated from the unwrapped phase, a differential interferometric strategy is employed for DEM generation [44]. This interferometric data processing strategy can reduce unwrapping errors and increase calculation efficiency particularly in case dense interferogram fringes [45].

Fig. 2 shows the flowchart of TanDEM-X DEM generation (as shown in dotted box) and glacier surface elevation changes estimation. Since the TDX data (CoSSC) were already coregistered, the main steps for TDX DEM generation are the following.

1) Step 1: Interferogram Generation and Topographic Phase Simulation: The interferogram (φ_{int}) is generated through the conjugate multiplication of two SLC SAR images. The interferogram can be multilooked for coherence estimation. The topographic phase $(\varphi_{\mathrm{SRTM}})$ is simulated based on the resulted height map and precise baseline product. In particular, since the TanDEM-X InSAR data is acquired in bistatic mode, the simulating interferometric phase for TSX/TDX configurations is different from repeat-pass configuration, and the simulated topographic phase from SRTM-C DEM can be calculated using the bistatic mode parameters. The differential phase $(\varphi_{\mathrm{diff}})$ is generated by removing the priori topographic phase $(\varphi_{\mathrm{SRTM}})$ from the interferogram using the following equation:

$$\varphi_{\mathrm{diff}} = \varphi_{\mathrm{int}} - \varphi_{\mathrm{SRTM}}. \quad (2)$$

2) Step 2: Coregistration Between SRTM DEM and TanDEM-X Data: The step of coregistration between SRTM-C DEM and TanDEM-X SAR images should be carried out before the processing of interferogran difference and filtering. Here we adopt the similar coregistration methods described in these literatures [22], [46]. First, an initial transformation function between the geographic coordinates of the SRTM-C DEM and the SAR coordinates of the TDX image, e.g., a geocoding lookup table of each grid, is established by using the imaging parameters and orbit information of the TDX scene, and a simulated SAR intensity image is generated from the SRTM-C DEM. Then, a bilinear polynomial model of horizontal offsets between the SRTM-simulated intensity and the TDX SAR intensity is generated using a cross-correlation optimization algorithm [47]. Third, the resultant polynomial model is used to refine the initial lookup table to accurately translate the SRTM-C DEM from the geographic coordinates to the respective TDX SAR coordinates. As results, the range shift and azimuth shift are 0.989 and 0.816 pixels, and the corresponding registration accuracy are 0.043 and 0.053 pixels according to a least-squares fit, respectively.

3) Step 3: Nonlocal (NL) Filtering of Differential Interferogram: The NL filter has been proven superior in noise suppression, resolution enhancement, and better coherence estimation for InSAR filtering [48]. In order to reduce noise influences on interferometric phase, the NL filter [48], comparing with Goldstein filter [49] used commonly, is applied to the differential interferogram. As the main parameters in the NL filter method, the equivalent number of looks, the radius of the search window size, and the half-width of the patches are set to 1, 12, and 5 in this paper, respectively. In addition, for the Goldstein filter method, the parameters of filtering window size, processing step, and exponent for nonlinear filtering are set to 32, 4, and 0.4, respectively. Then, differential phase unwrapping is carried out by using the minimum cost flow algorithm [50]. After differential phase is unwrapped, an updated topographic phase $(\varphi_{\mathrm{TDXtopo}})$ from TDX InSAR is generated by adding the priori topographic phase $(\varphi_{\mathrm{SRTM}})$ back to unwrapped differential phase $(\Delta\varphi_{\mathrm{unw}})$.

4) Step 4: TDX DEM Correction With ICESat Elevation Measurements: Since there is still a linear ramp in the $\varphi_{\mathrm{TDXtopo}}$ after the step of baseline refinement [44], a linear height ramp need to be removed. Therefore, in this study, independent ICESat elevation references with high vertical accuracy are used for this purpose. The selection criteria are fully detailed in [41]. The

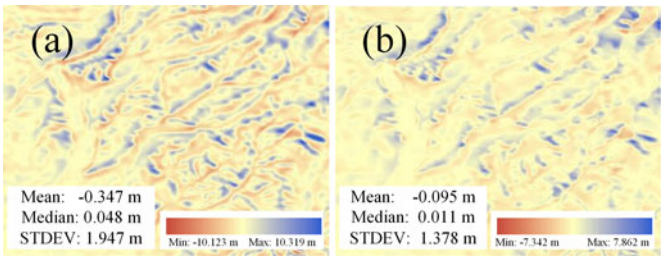

Fig. 3. Glacier elevation changes (a) before and (b) after the coregistration. Some statistics (mean, median, std. deviation) of two results of elevation changes are shown on this figure. This area is located at the blue dotted rectangle of Fig. 6.

height differences between the ICESat points and the raw TDX DEM are employed in a polynomial height correction model to acquire a linear ramp with a common least-squares solution. Furthermore, this linear height ramp in the raw TDX DEM can be removed to acquire the corrected TDX DEM.

B. Estimation of Glacier Elevation Changes

In this study, we use two different methods to estimate glacier elevation changes, named DiffDem and DiffPha. Fig. 2 shows processing flows of the two methods. Note that accurate coregistration between the SRTM DEM and the TDX datasets is mandatory before applying both methods, which is described more detailed in Section III-A. As an example, Fig. 3 illustrates a comparison of elevation changes results over a nonglacierized area before and after the coregistration. The statistical parameters of the elevation changes (see Fig. 3) show that the DEM coregistration process can improve the elevation change estimation, although residuals still exist in the results due to both the impact of SAR geometric distortion and the different resolution between two DEMs.

Once accurately coregistered, both DEMs in SAR coordinates have the same grid posting and are horizontally aligned, then the DiffDem method is applied to obtain glacier elevation changes between 2000 and 2013.

In addition, another method that directly exploits the unwrapped differential phase ($\Delta\varphi_{\mathrm{unw}}$), named the DiffPha method, is proposed to estimate elevation changes. The elevation change (ΔH) for each pixel can be computed using a simple algorithm based on the following equation:

$$\Delta H = -\frac{\lambda}{2\pi}\frac{R\sin(\theta_i)}{B_\perp}\cdot\Delta\varphi_{\mathrm{unw}} \tag{3}$$

where λ is the radar wavelength, $B_\perp$ is the perpendicular baseline for TSX/TDX, R is the slant range, and θ_i is the incidence angle for each pixel.

Finally, we use a statistical estimate of SRTM-C/X DEMs differences in adjacent glaciers, as a proxy of penetration depth difference between C-band and X-band radars, to correct elevation change results from SRTM-C and TanDEM-X DEMs, due to no SRTM-X DEMs or *in-situ* data available in our study area. Specifically, a total of 75 glaciers in Danghenan Mountains covered by 30 m SRTM-C DEM and SRTM-X DEM are selected for this purpose. This test site for radar penetration

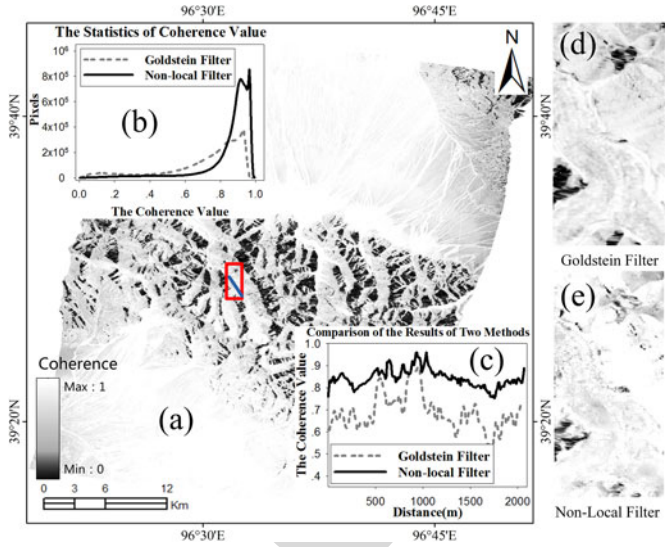

Fig. 4. Comparison of the coherence estimates with the Goldstein filter and NL filter. (a) The coherence result of TanDEM-X bistatic InSAR. (b) Histograms of the coherence results from different filters. (c) Coherence values along the profile line [blue line in Fig. 4(a)] for the results of two filters. (d) and (e) The coherence maps of Laohugou Glacier No.12 [red rectangle in Fig. 4(a)] with the Goldstein filter and the NL filter, respectively.

estimation is located 90 km southwest of the study area (see Fig. 1). The penetration differences between C-band SRTM DEM and X-band SRTM DEM are estimated using a common method of DEM differencing [7]. In the penetration difference analysis, we excluded glacier areas with slopes higher than 20°, resulting in a relatively reliable estimation of penetration depth difference. Consequently, the mean and standard deviation (1.470 ± 3.01 m) of the X-C-band SRTM penetration difference observed over glacier areas is used for correction of glacier elevation changes in this study.

C. Error Analysis

1) Accuracy Assessment of the TDX DEM: In order to quantitatively assess the TDX-derived DEM accuracy, we utilize a total of 1238 ICESat points from 2003 to 2009 which are located in off-glacier area (see Fig. 1). These ICESat measurements are independent from those used to correct TDX DEM during TanDEM-X DEM generation in Section III-A.

2) Uncertainty of Elevation Changes: In case of no *in-situ* measurements available, a common method for the overall error evaluation of elevation changes is used to calculate statistical errors of the elevation differences over nonglacier regions according to the following equation [51]:

$$e = \sqrt{\mathrm{NMAD}^2 + \mathrm{wRMSE}^2} \tag{4}$$

where e, NMAD, and wRMSE are the overall error of the derived surface glacier elevation changes, the random part of the error, and the systematic part of the error, respectively [22].

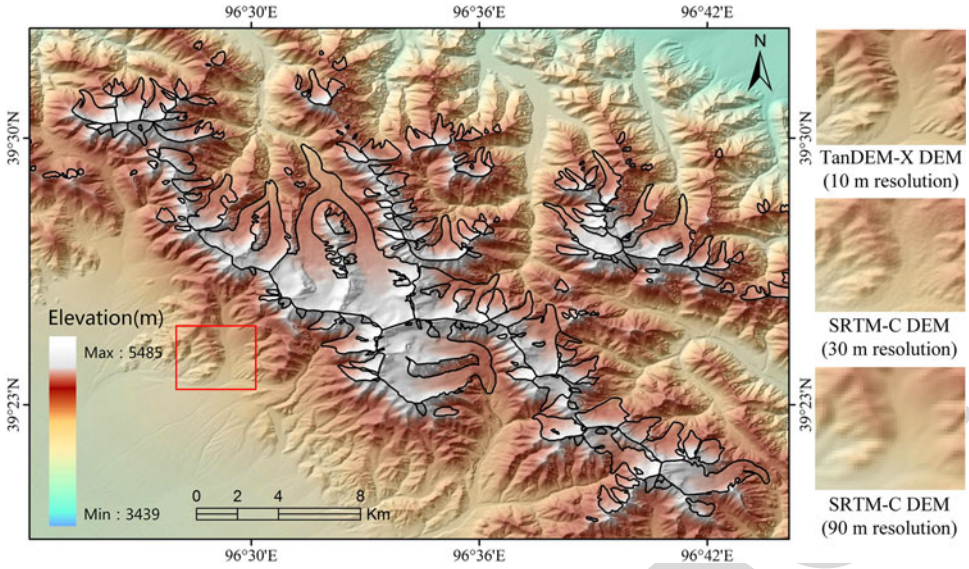

Fig. 5. 10 m resolution TanDEM-X DEM generated by TDX bistatic InSAR (left). Comparisons of the 10 m TanDEM-X DEM, 30 m SRTM-C DEM, and 90 m SRTM-C DEM are shown in the right part.

IV. Results and Analysis

A. Comparison of Coherence Estimation From Different Filters

Since coherence is one of the key parameters to evaluate interferometric performance, which represents a noise level in the interferogram, we analyze and compare the TDX InSAR conference results from the NL and Goldstein filters as shown in Fig. 4. Overall, the mean value of coherence reaches 0.88, even in glacier area up to 0.80, although the coherence in shadow regions is slightly lower due to very low backscatter.

A comparison of coherence results indicates that the NL filter can present a better performance of coherence estimation than the Goldstein filter. Statistically, the coherence value is mainly concentrated in the ranges of 0.8–1.0 using the NL filter, whereas ranging from 0.6 to 1.0 for the Goldstein filter, see Fig. 4(b). Moreover, coherence values along a profile line in the Laohugou Glacier No. 12 [a blue line in the red rectangle in Fig. 4(a)] clearly show that most of coherence values of the NL filter are 0.2 higher than the Goldstein filter, see Fig. 4(c). In order to further compare the ability of phase noise reduction and fine detail preservation, Fig. 4(d) and (e) illustrates Laohugou Glacier No.12 subset of coherence maps of the two filters, respectively. Visually, the NL filter presents generally higher coherence (brighter) and more details than the Goldstein filter.

B. TDX-Derived DEM and Validation

Fig. 5 illustrates the hillshade map of the TDX DEM derived by bistatic InSAR with the NL filter. In order to visually compare differences between TDX and SRTM-C DEMs, the 10 m TDX, 30 m, and 90 m SRTM-C DEMs (located in the red rectangle in Fig. 5) are shown from top to bottom on the right side of Fig. 5, respectively. As a consequence, the 10 m TDX DEM represents much more detailed topographic information, such as clear river channel, than the SRTM DEM. Moreover, quantitative accuracy assessments of the InSAR-derived TDX DEMs using the two different filters have been performed. Table II shows the statistical result of DEM accuracy assessment for TanDEM-X DEM with ICESat measurements. We find a mean and root mean square error (RMSE) of 1.493 ± 0.747 m for the NL filter, whereas 1.857 ± 1.709 m for the Goldstein filter. In addition, much higher error ranges (from –17.343 to 13.928 m) are found in the Goldstein filter's results.

TABLE II
Statistical Results of Difference Between the ICESat Height Measurements and the TDX DEMs Derived With Two Different Filters

Statistical parameters	Goldstein filter	NL filter
Min (m)	−17.343	−1.554
Max (m)	13.928	2.510
Mean (m)	1.857	1.493
RMSE (m)	1.709	0.747

Overall, for this study, the TDX DEM can reach the HRTI-3 standards with the resolution of 10 m and the vertical accuracy of 0.75 m for off-glacier regions [19], which is the first high-resolution and high-accuracy DEM in the western Qilian Mountain glaciated terrain, although the elevation in high-relief areas appears coarse due to the shadow influences. Theoretically, the vertical accuracy of the TDX DEM in glacier regions is worse than that of off-glacier regions, due to the interferometric bias induced by X-band radar penetration into snow and ice [52].

C. Glacier Elevation Changes

In this study, glacier elevation changes between 2000 and 2013 over the western Qilian Mountain are calculated from

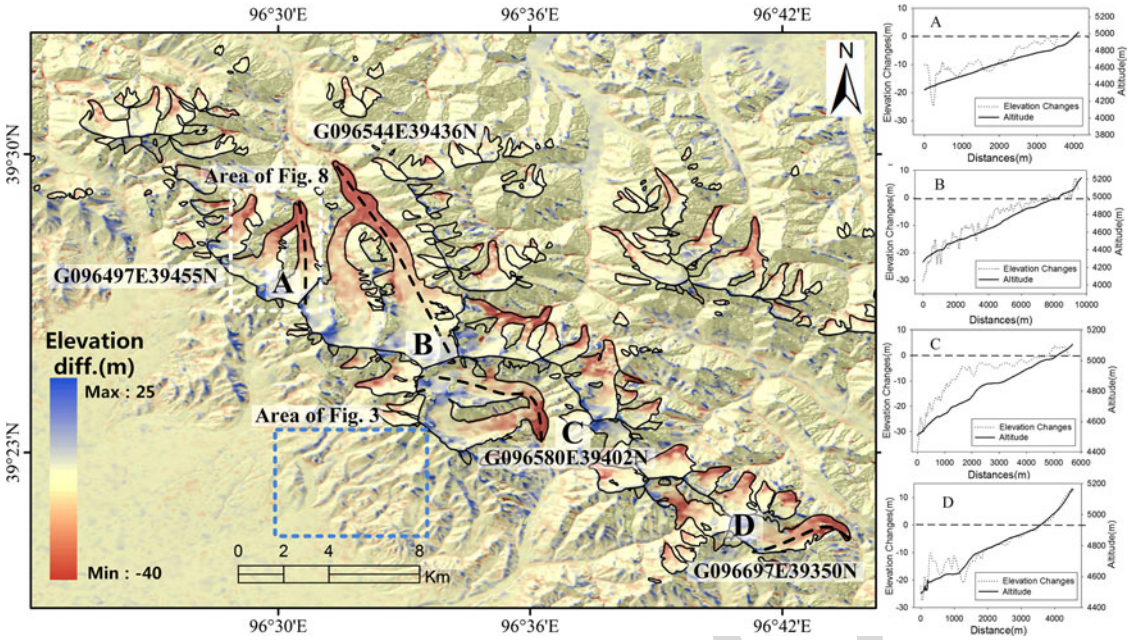

Fig. 6. Glacier elevation changes in the western Qilian Mountain derived by synergistic use of the DiffPha method and the NL filter. The white-dotted rectangle indicates the location of the glacier G096497E39455N, elevation changes of which are illustrated in Fig. 8. The correlation between the elevation changes and the altitudes along profile lines of the selected four glaciers in the right part. (A) G096497E39455N; (B) G096544E39436N; (C) G096580E39402N; and (D) G096697E39350N.

SRTM-C DEM and TanDEM-X bistatic data, by using four approaches in terms of different combinations of elevation change estimation methods (DiffDem method and DiffPha method) and filtering algorithms (Goldstein filter and NL filter). Here we illustrate the elevation change results derived by synergistic use of the DiffPha method and the NL filter (see Fig. 6), as this method is superior to other three ones examined by a performance comparison described in the next paragraph. The glacier boundaries (the black solid lines in Fig. 6) generated from the Second Glacier Inventory Dataset of China [27] are used to clearly exhibit elevation changes over glacier regions. Generally, we detected a clear surface thinning pattern in most glacier tongue regions, with a maximum elevation lowering up to approximately –40 m, whereas a slight thickening was detected in accumulation areas. In order to examine this elevation change pattern in more details, we calculate height differences between the GPS measurements at Laohugou Glacier No.12 collected in 2012 and the SRTM-C DEM at corresponding locations. Fig. 7 illustrates altitude dependence of two groups of elevation change results derived from TDX DEM minus SRTM DEM (TDX-SRTM) and GPS minus SRTM DEM (GPS-SRTM), respectively. The two groups of results have a consistent trend over the past decades, in which more significant glacier melting occurred in the ablation areas with lower altitudes, whereas glacier surface change was less at higher elevation. This could be interpreted as a result of increased mean temperature in summer and decreased annual total precipitation that were recorded by field measurement in the western Qilian Mountains during the past decades [53], [54]. In addition, there are still slight differences between two groups of elevation change results, which might be attributed to the data sets of different time

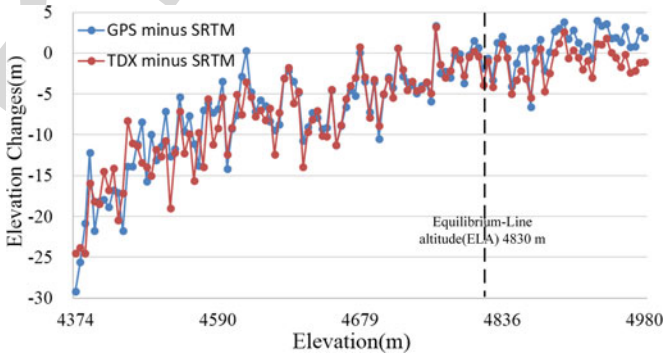

Fig. 7. Relation between altitude and elevation changes of the Laohugou Glacier No.12 derived from TDX DEM minus SRTM DEM and GPS minus SRTM DEM, respectively.

periods as well as the accuracy differences of differing instruments. Furthermore, we estimate the mean elevation change of -2.823 ± 1.065 m for the whole glacier area, and the rate of mass depletion is -195.44 ± 73.82 mm w.eq.a^{-1} with the ice density of 900 ± 17 kg m^{-3} [22].

We evaluate uncertainty of these four different approaches used for elevation change estimation, by calculating the statistical errors of elevation changes over the nonglacier regions with (4), as shown in Table III. In general, the DiffPha method slightly surpasses the DiffDem method, since the former has smaller statistical values of three error parameters (see Table III). This might be due to the DiffPha method directly estimate the elevation changes from unwrapped differential phases and therefore it is not or less influenced by error sources involved in DiffDem method such as absolute height offset correction and

TABLE III
STATISTICAL ERRORS OF ELEVATION CHANGES OVER NONGLACIER REGIONS FOR FOUR APPROACHES

Methods	wRMSE (m)	NMAD (m)	e (m)
DiffPha with the Goldstein filter	1.014	0.591	1.174
DiffPha with the NL filter	0.912	0.550	1.065
DiffDem with the Goldstein filter	1.350	0.845	1.593
DiffDem with the NL filter	1.213	0.715	1.408

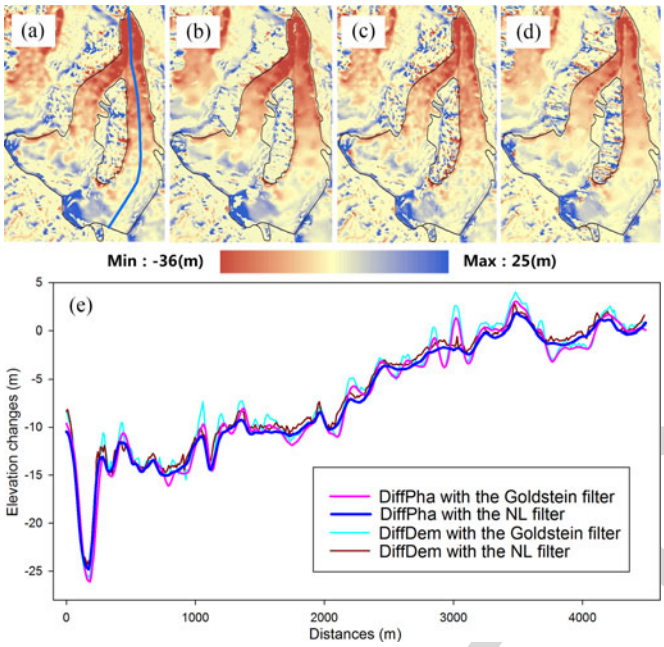

Fig. 8. Comparison of elevation change results of the glacier G096497E39455N (the location is shown in Fig. 6). (a) DiffPha method with the Goldstein filter; (b) DiffPha method with the NL filter; (c) DiffDem method with the Goldstein filter; (d) DiffDem method with the NL filter; (e) profiles of elevation change results of four methods used in this study from glacier terminus [the blue line in (a) is the location of profiles].

DEM coregistration. Additionally, the NL filter is superior to the Goldstein filter, and the least overall error of 1.065 m is found in the glacier elevation change result by synergistic use of the Diffpha method and the NL filter. This might benefit from better performances of noise reduction, detail preservation, and coherence estimation from the NL filtering [48].

Moreover, Fig. 8 illustrates the results over a glacier (No.G096497E39455N) from the four approaches of elevation change estimation, which is located in the dotted white rectangle in Fig. 6. First, the results of the DiffPha methods [see Fig. 8(a) and (b)] are better than those of the DiffDem methods [see Fig. 8(c) and (d)] in the aspect of noise reduction. The DiffDem methods seem to preserve more details in the glacier interior than the DiffPha methods, however, these false details of elevation changes in Fig. 8(c) and (d) might be the noise from the lower resolution of SRTM-C DEM which is used twice again after the differential phase is filtered (see Fig. 2). However, in the DiffPha-based approaches, the filtered unwrapped differential phases are directly translated to elevation changes and are less affected by this SRTM-C DEM noises. Second, through comparison of Fig. 8(a) and (b), the NL filter has a better performance for noise reduction than the Goldstein filter. This superior of the DiffPha method along with the NL filter is also illustrated in comparisons of elevation changes along a profile of the glacier, as shown in Fig. 8(e).

D. Correlation Between Glacier Elevation Changes and Altitude

The local response of individual glaciers differs (see Fig. 6) and the elevation changes show moderate spatial variations that are mainly determined by glacier altitude, glacier slop, glacier aspect, and glacier dynamics [55]. In order to analyze the correlation between glacier elevation changes and altitude, we selected four largest glaciers in this study area as shown in Fig. 6, which are the glaciers numbered with G096497E39455N, G096544E39436N, G096580E39402N, and G096697E39350N, respectively. Fig. 6 in the right part shows the glacier elevation changes with the altitude along the profiles for each selected glacier. We can find a definite trend of negative correlation between glacier elevation changes and corresponding altitudes for each glacier, inferring that the glacier altitude is one of key local controls on glacier mass balance in this area.

V. DISCUSSION

The penetration of the radar signals into snow and ice remains one of the major sources of uncertainty when using InSAR-derived DEMs to estimate geodetic glacier mass balance [7], [56]. Recently, an analysis of elevation changes derived from radar and optical DEMs suggests that at accumulation areas above 4000 m a.s.l. the TDX penetration can reach 4 m on average in October and February, corresponding to a geodetic mass balance bias of ∼1.66 m w.e. in an alpine glacier [25]. It implies that this systematic error due to the radar penetration might limit the use of the TDX DEM to derive glacier annual mass balances when compared with DEM products from other sources, e.g., optical stereo images or Lidar point clouds.

In this study, our focus is mainly on correction of the interferometric penetration difference between C-band and X-band radar signals into glacier areas. Actually, a quantitative analysis of elevation change uncertainty caused by this radar penetration difference is a large challenge when comparing the DEMs generated from InSAR data acquired with different-wavelength radars. A usual method is that a penetration depth value for a certain wavelength of radar signal reported in literatures is used as a proxy to reduce the influence of radar penetration on glacier elevation change estimation [37]. In this study, we adopted a more realistic method for compensating the penetration difference between SRTM-C and TDX radar signals. Due to no X-band SRTM DEM available in the study area, a pair of SRTM-C/X DEMs over the Danghenan Mountain glaciers which was located 90 km southwest of the study area, was selected to statistically estimate penetration differences. Indeed, this penetration depth of radar signals might be influenced by the various terrain and snow conditions over different areas.

However, the two glaciated regions have similar glacier terrain and morphologic features (e.g., altitude ranges, glacier aspect) as well as comparable climatic conditions (annual precipitations and temperatures) [57], therefore it might imply a similar influence of radar penetration on elevation change estimation for the two sites. Consequently, the mean value (1.470 m) of radar penetration differences was used for correcting glacier elevation change in this study. This statistical estimation is generally consistent with the literature [7], who reported mean values (varying from 1.4 to 3.4 m) of the penetration difference between the X-band and C-band SRTM DEMs for different glaciers in the Pamir–Karakoram–Hengduan Shan regions.

In addition, we estimate the standard deviation of approximately $\pm$ 3.01 m for the penetration differences between X-band and C-band radars over the observed glacier areas, which agreed generally with those reported in the previous studies [58]–[60]. In most cases of mountain glaciers, this standard deviation might be relatively high which value is usually in order of some meters, due to highly variable penetration depths which strongly depend on glacier zone (altitude) and snow/firn/ice properties [61]. Therefore, if the variation of penetration difference is considered as a term of uncertainty estimation for elevation changes, the uncertainty value should be larger than that in case of not considered. For instance, in our study the uncertainty value of elevation change increases to 3.17 from 1.01 m as obtained only according to (4). This also implies that the uncertainty of mass balance might be underestimated in several studies which neglected this term in their uncertainty estimation for glacier thickness changes [7], [62], [63].

VI. Conclusion

The presented study demonstrates that TSX/TDX bistatic InSAR is a promising satellite remotely sensing method for monitoring surface topography and elevation changes in mountain glacierized regions. The first high-resolution and high-precision glacier surface topography in the western Qilian Mountain has been measured by using the TanDEM-X InSAR dataset acquired in November 2013. The accuracy assessment of the TDX-derived DEM with ICESat elevation data in flat off-glacier areas demonstrates that the NL filter is superior to the Goldstein filter in InSAR DEM generation and the absolute height accuracy is improved from 1.857 $\pm$ 1.709 m to 1.493 $\pm$ 0.747 m. Note that this superiority of the NL filter versus the Goldstein filter is only for the parameters investigated in this study and more assessment investigations are needed. In addition, the DiffPha method and the DiffDem method have been applied to estimate glacier elevation changes between the derived TDX DEM and the C-band SRTM DEM. Results show that the former surpasses slightly the later and the overall error is found to be 1.065 m in the results of glacier elevation change derived by synergistic use of the DiffPha method and the NL filter. We estimate mean elevation change of -2.823 ± 1.065 m for the whole glacier area, and the rate of mass depletion is –195.44 $\pm$ 73.82 mm w.eq.a^{-1}. A clear surface thinning pattern can be found in most glacier tongue regions, with a maximum value of elevation lowering up to approximately -40 m, whereas a slight thickening was detected in accumulation areas. The glacier changes are generally in agreement with the height difference results between GPS measurements and SRTM-C DEM.

Acknowledgment

The authors would like to thank anonymous reviewers for their valuable comments and suggestions that greatly improved the quality of this paper, USGS for providing the SRTM DEM used, and Mr. Y. Wang at Northwest Institute of Eco-Environment and Resources (CAS) for the helpful discussions in the result interpretation and for providing the GPS measurements.

References

[1] A. E. Racoviteanu, W. F. Manley, and Y. Arnaud, "Evaluating digital elevation models for glaciologic applications: An example from Nevado Coropuna, Peruvian Andes," *Global Planet. Change*, vol. 59, no. 1, pp. 110–125, Jan. 2007.

[2] D. Scherler, B. Bookhagen, and M. R. Strecker, "Spatially variable response of Himalayan glaciers to climate change affected by debris cover," *Nature Geosci.*, vol. 4, no. 3, pp. 156–159, Jan. 2011.

[3] R. Bhambri, T. Bolch, and R. Chaujar, "Mapping of debris-covered glaciers in the Garhwal Himalayas using ASTER DEMs and thermal data," *Int. J. Remote Sens.*, vol. 32, no. 23, pp. 8095–8119, Sep. 2011.

[4] T. Bolch, M. Buchroithner, and T. Pieczonka, "Planimetric and volumetric glacier changes in the Khumbu Himal, Nepal, since 1962 using Corona, Landsat TM and ASTER data," *J. Glaciol.*, vol. 54, no. 187, pp. 592–600, Dec. 2008.

[5] T. Bolch, A. Kulkarni, and A. Kääb, "The state and fate of Himalayan glaciers," *Science*, vol. 336, no. 6079, pp. 310–314, Apr. 2012.

[6] E. Berthier, E. Schiefer, and G. Clarke, "Contribution of Alaskan glaciers to sea-level rise derived from satellite imagery," *Nature Geosci.*, vol. 3, no. 2, pp. 92–95, Jan. 2010.

[7] J. Gardelle, E. Berthier, and Y. Arnaud, "Region-wide glacier mass balances over the Pamir-Karakoram-Himalaya during 1999-2011," *Cryosphere*, vol. 7, no. 6, pp. 1885–1886, Aug. 2013.

[8] D. Lamsal, T. Sawagaki, and T. Watanabe, "Digital terrain modelling using Corona and ALOS PRISM data to investigate the distal part of Imja Glacier, Khumbu Himal, Nepal," *J. Mountain Sci.*, vol. 8, no. 3, pp. 390–402, Jun. 2011.

[9] X. Tang, G. Zhang, and X. Zhu, "Triple linear-array image geometry model of ZiYuan-3 surveying satellite and its validation," *Int. J. Image Data Fusion*, vol. 4, no. 1, pp. 33–51, Mar. 2013.

[10] T. Toutin, C. Schmitt, and E. Berthier, "DEM generation over ice fields in the Canadian Arctic with along-track SPOT5 HRS stereo data," *Can. J. Remote Sens.*, vol. 37, no. 4, pp. 429–438, Feb. 2012.

[11] D. J. Quincey, M. Bishop, and A. Kääb, "Digital terrain modeling and glacier topographic characterization," in *Global Land Ice Measurements From Space*. Berlin, Germany: Springer, 2014, pp. 113–144.

[12] P. Rosen, "Synthetic aperture radar interferometry," *Proc. IEEE*, vol. 88, no. 3, pp. 333–382, Mar. 2000.

[13] K. Eldhuset, P. H. Andersen, and S. Hauge, "ERS tandem InSAR processing for DEM generation, glacier motion estimation and coherence analysis on Svalbard," *Int. J. Remote Sens.*, vol. 24, no. 7, pp. 1415–1437, Jun. 2003.

[14] X. Peng, J. Wang, and Q. Zhang, "Deriving terrain and textural information from stereo RADARSAT data for mountainous land cover mapping," *Int. J. Remote Sens.*, vol. 26, no. 22, pp. 5029–5049, Mar. 2005.

[15] C. Thiel and C. Schmullius, "Impact of tree species on magnitude of PALSAR interferometric coherence over Siberian forest at frozen and unfrozen conditions," *Remote Sens.*, vol. 26, no. 22, pp. 1124–1136, Jan. 2014.

[16] S. Hensley, C. Jones, and D. Moller, "Ice studies using UAVSAR L-band and Ka-band data," in *Proc. 8th Eur. Conf. Synt. Aperture Radar*, Aachen, Germany, Jun. 2010, pp. 1–4.

[17] P. Pellikka and W. G. Rees, *Remote Sensing of Glaciers: Techniques for Topographic, Spatial and Thematic Mapping of Glaciers*. Boca Raton, FL, USA: CRC Press, 2010.

[18] T. G. Farr, P. A. Rosen, and E. Caro, "The shuttle radar topography mission," *Rev. Geophys.*, vol. 45, no. 2, pp. 1–33, May 2007.

[19] G. Krieger, A. Moreira, and H. Fiedler, "TanDEM-X: A satellite formation for high-resolution SAR interferometry," *IEEE Trans. Geosci. Remote Sens.*, vol. 45, no. 11, pp. 3317–3341, Oct. 2007.

[20] G. Li and H. Lin, "Recent decadal glacier mass balances over the western Nyainqentanglha Mountains and the increase in their melting contribution to Nam Co Lake measured by differential Bistatic SAR interferometry," *Global Planet. Change*, vol. 149, pp. 177–190, Feb. 2017.

[21] G. Liu, J. Fan, F. Zhao, and K. Mao, "Monitoring elevation change of glaciers on Geladandong Mountain using TanDEM-X SAR interferometry," *J. Mountain Sci.*, vol. 14, no. 5, pp. 859–869, 2017.

[22] N. Neckel and A. Braun, "Recent mass balance of the Purogangri Ice Cap, central Tibetan Plateau, by means of differential X-band SAR interferometry," *Cryosphere*, vol. 7, no. 5, pp. 1623–1633, Oct. 2013.

[23] L. Liu, L. M. Jiang, and Y. F. Sun, "Glacier elevation changes (2012–2016) of the Puruogangri ice field on the Tibetan Plateau derived from bi-temporal TanDEM-X InSAR data," *Int. J. Remote Sens.*, vol. 37, no. 24, pp. 5687–5707, Oct. 2016.

[24] J. Li, Z. Li, and J. Zhu, "Early 21st century glacier thickness changes in the Central Tien Shan," *Remote Sens. Environ.*, vol. 192, pp. 12–29, Feb. 2017.

[25] A. Dehecq, R. Millan, and E. Berthier, "Elevation changes inferred from TanDEM-X data over the Mont-Blanc area: Impact of the x-band interferometric bias," *IEEE J. Sel. Topics Appl. Earth Observ. Remote Sens.*, vol. 9, no. 8, pp. 3870–3882, Jul. 2016.

[26] H. Rott, "Mass changes of outlet glaciers along the Nordensjköld Coast, northern Antarctic Peninsula, based on TanDEM-X satellite measurements," *Geophys. Res. Lett.*, vol. 41, no. 22, pp. 8123–8129, Nov. 2014.

[27] W, Guo, J. L. Xu, and S. Y. Liu, "The second glacier inventory dataset of China (Version 1.0)," Cold and Arid Regions Science Data Center: Lanzhou, China, 2014.

[28] Y. Zhang, S. Liu, and D. Shangguan, "Thinning and shrinkage of Laohugou No. 12 glacier in the Western Qilian Mountains, China, from 1957 to 2007," *J. Mountain Sci.*, vol. 9, no. 3, pp. 343–350, Jun. 2012.

[29] Y. S. Liu, X. Qin, and S. Gao, "Accuracy evaluation of glacier area information extracted from Landsat-5 TM remote sensing image," *J. Northwest A&F Univ. (Natural Sci. Ed.)*, vol. 41, no. 12, pp. 209–219, 2013.

[30] G. B. Yu, Z. Q. Li, and P. Y. Wang, "Glacier changes at the Daxue Mountain and Danghenan Mountain of west Qilian Mountains in recent 50 years," (in Chinese), *Arid Land Geophys.*, vol. 37, no. 2, pp. 299–309, Mar. 2014.

[31] J. Z Chen, "Simulating the energy and mass balances on the Laohugou Glacier No. 12 in the Qilian Mountains," (in Chinese), *J. Glaciol. Geocryol.*, vol. 36, no. 1, pp. 38–47, Feb. 2014.

[32] W. Sun, X. Qin, and Y. Xu, "Annual variations of the components of radiation on the Laohugou No.12 glacier in the Qilian mountains," (in Chinese), *Adv. Earth Sci.*, vol. 26, no. 3, pp. 347–354, Mar. 2011.

[33] Y. Wang, T. Zhang, and J. Ren, "An investigation of the thermo-mechanical features of Laohugou Glacier No.12 in Mt. Qilian Shan, western China, using a two-dimensional first-order flow-band ice flow model," *Cryosphere Discuss.*, Mar. 2016.

[34] W. Du, X. Qin, and Y. Liu, "Variation of the laohugou glacier No.12 in the qilian mountains," (in Chinese), *J. Glaciol. Geocryol.*, vol. 30, no. 3, pp. 373–379, Jun. 2008.

[35] M. J. Zhang, "Glacier change in the Laohugou river basin monitored by remote sensing from 1957 to 2009," (in Chinese), *J. Arid Land Resour. Environ.*, vol. 27, no. 4, pp. 70–75, Apr. 2013.

[36] I. Hajnsek and T. Busche, "TanDEM-X science plan," DLR, Cologne, Germany, DLR Public Document TD-PD-PL-0069, 2010.

[37] E. Berthier and Y. Arnaud, "Biases of SRTM in high-mountain areas: Implications for the monitoring of glacier volume changes," *Geophys. Res. Lett.*, vol. 33, no. 8, pp. 1–5, Apr. 2006.

[38] A. Kääb, "Combination of SRTM3 and repeat ASTER data for deriving alpine glacier flow velocities in the Bhutan Himalaya," *Remote Sens. Environ.*, vol. 94, no. 4, pp. 463–474, Feb. 2005.

[39] X. Huang, H. Xie, and T. Liang, "Estimating vertical error of SRTM and map-based DEMs using ICESat altimetry data in the eastern Tibetan Plateau," *Int. J. Remote Sens.*, vol. 32, no. 18, pp. 5177–5196, Aug. 2011.

[40] M. Huber, B. Wessel, and D. Kosmann, "Ensuring globally the TanDEM-X height accuracy: Analysis of the reference data sets ICESat, SRTM and KGPS-tracks," in *Proc. IEEE Int. Geosci. Remote Sens. Symp.*, Cape Town, South Africa, Jul. 2009, pp. II-769–II-772.

[41] J. H. González, M. Bachmann, and R. Scheiber, "Definition of ICESat selection criteria for their use as height references for TanDEM-X," *IEEE Trans. Geosci. Remote Sens.*, vol. 48, no. 6, pp. 2750–2757, Jun. 2010.

[42] A. Ferretti, C. Prati, and F. Rocca, "Permanent scatterers in SAR interferometry," *IEEE Trans. Geosci. Remote Sens.*, vol. 39, no. 1, pp. 8–20, Jan. 2001.

[43] J. H. González, J. Antony, and M. Bachmann, "Bistatic system and baseline calibration in TanDEM-X to ensure the global digital elevation model quality," *ISPRS J. Photogramm. Remote Sens.*, vol. 73, no. 1, pp. 3–11, Jun. 2012.

[44] A. Gruber, B. Wessel, and M. Huber, "Operational TanDEM-X DEM calibration and first validation results," *ISPRS J. Photogramm. Remote Sens.*, vol. 73, no. 1, pp. 39–49, Jun. 2012.

[45] H. Jiang, L. Zhang, and Y. Wang, "Fusion of high-resolution DEMs derived from COSMO-SkyMed and TerraSAR-X InSAR datasets," *J. Geodesy*, vol. 88, no. 6, pp. 587–599, Jun. 2014.

[46] M. Rankl and M. Braun, "Glacier elevation and mass changes over the central Karakoram region estimated from TanDEM-X and SRTM/X-SAR digital elevation models," *Ann. Glaciol.*, vol. 57, no. 71, pp. 273–281, Mar. 2016.

[47] J. Kropáček, G. Grandi, and Y. Rauste, "Geo-referencing of continental-scale JERS-1 SAR mosaics based on matching homologous features with a digital elevation model: Theory and practice," *Int. J. Remote Sens.*, vol. 33, no. 8, pp. 2413–2433, Oct. 2012.

[48] C. A. Deledalle, L. Denis, and F. Tupin, "NL-InSAR: Nonlocal interferogram estimation," *IEEE Trans. Geosci. Remote Sens.*, vol. 49, no. 4, pp. 1441–1452, Apr. 2011.

[49] R. M. Goldstein and C. L. Werner, "Radar interferogram filtering for geophysical applications," *Geophys. Res. Lett.*, vol. 25, no. 21, pp. 4035–4038, Nov. 1998.

[50] M. Costantini, "A novel phase unwrapping method based on network programming," *IEEE Trans. Geosci. Remote Sens.*, vol. 36, no. 3, pp. 813–821, May 1998.

[51] T. Koblet, "Reanalysis of multi-temporal aerial images of Storglaciären, Sweden (1959–99)–Part 1: Determination of length, area, and volume changes," *Cryosphere*, vol. 4, no. 3, pp. 333–343, Sep. 2010.

[52] W. Hoen and H. Zebker, "Penetration depths inferred from interferometric volume decorrelation observed over the Greenland ice sheet," *IEEE Trans. Geosci. Remote Sens.*, vol. 38, no. 6, pp. 2571–2583, Nov. 2000.

[53] X. Qin, J. Chen, and S. Wang, "Reconstruction of surface air temperature in a glaciated region in the western Qilian Mountains, Tibetan Plateau, 1957–2013 and its variation characteristics," *Quaternary Int.*, vol. 371, pp. 22–30, Nov. 2015.

[54] X. Qin, X. Cui, and W. Du, "Variations of the alpine precipitation from an ice core record of the Laohugou glacier basin during 1960–2006 in western Qilian Mountains, China," *J. Geographical Sci.*, vol. 25, no. 2, pp. 165–176, May 2015.

[55] A. E. Racoviteanu, Y. Arnaud, and M. W. Williams, "Spatial patterns in glacier characteristics and area changes from 1962 to 2006 in the Kanchenjunga-Sikkim area, eastern Himalaya," *Cryosphere*, vol. 9, no. 1, pp. 505–523, Mar. 2015.

[56] C. Nuth and A. Kääb, "Co-registration and bias corrections of satellite elevation data sets for quantifying glacier thickness change," *Cryosphere*, vol. 5, pp. 271–290, Mar. 2011.

[57] P. Wang, Z. Li, and G. Yu, "Glacier shrinkage in the Daxue and Danghenan ranges of the western Qilian Mountains, China, from 1957 to 2010," *Environ. Earth Sci.*, vol. 75, no. 2, pp. 1–11, Jan. 2016.

[58] R. Muskett, S. Lingle, and M. Sauber, "Airborne and spaceborne DEM- and laser altimetry-derived surface elevation and volume changes of the Bering Glacier system, Alaska, USA, and Yukon, Canada, 1972–2006," *J. Glaciol.*, vol. 55, no. 190, pp. 316–326, Apr. 2009.

[59] E. Rignot, K. Echelmeyer, and W. Krabill, "Penetration depth of interferometric synthetic-aperture radar signals in snow and ice," *Geophys. Res. Lett.*, vol. 28, no. 18, pp. 3501–3504, Sep. 2001.

[60] K. Melkonian, J. Willis, and E. Pritchard, "Satellite-derived volume loss rates and glacier speeds for the Cordillera Darwin Icefield, Chile," *Cryosphere*, vol. 7, no. 3, pp. 823–839, May 2013.

[61] B. Surazakov and B. Aizen, "Estimating volume change of mountain glaciers using SRTM and map-based topographic data," *IEEE Trans. Geosci. Remote Sens.*, vol. 44, no. 10, pp. 2991–2995, Oct. 2006.

[62] J. Gardelle, E. Berthier, and Y. Arnaud, "Slight mass gain of Karakoram glaciers in the early twenty-first century," *Nature Geosci.*, vol. 5, no. 5, pp. 322–325, May 2012.

[63] J. Willis, K. Melkonian, and E. Pritchard, "Ice loss from the southern patagonian ice field, south America, between 2000 and 2012," *Geophys. Res. Lett.*, vol. 39, no. 17, pp. 1–6, Sep. 2012.

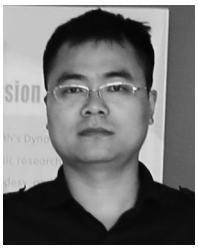

Yafei Sun received the B.S. degree in surveying and mapping engineering from the Taiyuan University of Technology, Taiyuan, China, in 2010 and the M.S. degree in geodetic and surveying engineering from the Institute of Geodesy and Geophysics, Chinese Academy of Sciences, Wuhan, China, in 2014. He is currently working toward the Ph.D. degree in geodetic and surveying engineering at the Chinese Academy of Sciences.

His research interests include TanDEM-X bistatic InSAR and glacier mass balance.

Liming Jiang received the B.S. degree in surveying and mapping engineering from Chang'an University, Xi'an, China, in 2000, the M.S. degree in remote sensing and GIS from Chengdu University of Technology, Chengdu, China, in 2003, and the Ph.D. degree in photogrammetry and remote sensing from Wuhan University, Wuhan, China, in 2006.

He is currently a Professor at the Institute of Geodesy and Geophysics, Chinese Academy of Sciences, Wuhan. His research interests include imaging geodesy, InSAR, and remote sensing of the cryosphere.

Lin Liu received the B.S. degree in surveying and mapping engineering from China University of Petroleum, Dongying, China, in 2006, the M.S. degree in photogrammetry and remote sensing from Wuhan University, Wuhan, China, in 2008, and the Ph.D. degree in geodetic and surveying engineering from the Chinese Academy of Sciences, Wuhan, in 2016.

His research interests include multitemporal SAR processing algorithms and its application in glacier dynamics.

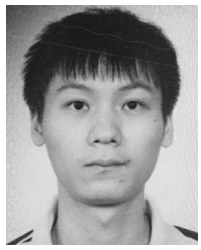

Qishi Sun received the B.S. degree in photogrammetry and remote sensing from the Chang'an University, Xi'an, China, in 2000. He is currently working toward the Ph.D. degree in geodetic and surveying engineering at the Chinese Academy of Sciences, Wuhan, China.

His research interests include nonlocal means filtering and time-series InSAR.

Hansheng Wang received the B.S. and M.S. degrees in applied geophysics from China University of Geosciences, Wuhan, China, in 1984 and 1989, respectively, and the Ph.D. degree in solid earth physics from the Institute of Geodesy and Geophysics, Chinese Academy of Sciences, Wuhan, in 1999.

He is currently a Professor at the Institute of Geodesy and Geophysics, Chinese Academy of Sciences. His research interests include GIA model and InSAR.

Houtse Hsu received the B.S. degree in geodetic and surveying engineering from Tongji University, Shanghai, China, in 1955, and the M.S. degree in geodetic and surveying engineering from the Institute of Geodesy and Geophysics, Chinese Academy of Sciences, Wuhan, China, in 1962.

He is currently an Academician at the Chinese Academy of Sciences. His research interests include geodesy and geophysics.